VA-DEPTHNET: A VARIATIONAL APPROACH TO SINGLE IMAGE DEPTH PREDICTION

Ce Liu[1] **Suryansh Kumar**[1*] **Shuhang Gu**[2] **Radu Timofte**[1,3] **Luc Van Gool**[1,4]
[1]CVL ETH Zürich [2]UESTC China [3]University of Würzburg [4]KU Leuven
{ce.liu, sukumar, vangool}@vision.ee.ethz.ch
shuhanggu@uestc.edu.cn, radu.timofte@uni-wuerzburg.de

ABSTRACT

We introduce VA-DepthNet, a simple, effective, and accurate deep neural network approach for the single-image depth prediction (SIDP) problem. The proposed approach advocates using classical first-order variational constraints for this problem. While state-of-the-art deep neural network methods for SIDP learn the scene depth from images in a supervised setting, they often overlook the invaluable invariances and priors in the rigid scene space, such as the regularity of the scene. The paper's main contribution is to reveal the benefit of classical and well-founded variational constraints in the neural network design for the SIDP task. It is shown that imposing first-order variational constraints in the scene space together with popular encoder-decoder-based network architecture design provides excellent results for the supervised SIDP task. The imposed first-order variational constraint makes the network aware of the depth gradient in the scene space, i.e., regularity. The paper demonstrates the usefulness of the proposed approach via extensive evaluation and ablation analysis over several benchmark datasets, such as KITTI, NYU Depth V2, and SUN RGB-D. The VA-DepthNet at test time shows considerable improvements in depth prediction accuracy compared to the prior art and is accurate also at high-frequency regions in the scene space. At the time of writing this paper, our method—labeled as VA-DepthNet, when tested on the KITTI depth-prediction evaluation set benchmarks, shows state-of-the-art results, and is the top-performing published approach[1] [2].

1 INTRODUCTION

Over the last decade, neural networks have introduced a new prospect for the 3D computer vision field. It has led to significant progress on many long-standing problems in this field, such as multi-view stereo (Huang et al., 2018; Kaya et al., 2022), visual simultaneous localization and mapping (Teed & Deng, 2021), novel view synthesis (Mildenhall et al., 2021), etc. Among several 3D vision problems, one of the challenging, if not impossible, to solve is the single-image depth prediction (SIDP) problem. SIDP is indeed ill-posed—in a strict geometric sense, presenting an extraordinary challenge to solve this inverse problem reliably. Moreover, since we do not have access to multi-view images, it is hard to constrain this problem via well-known geometric constraints (Longuet-Higgins, 1981; Nistér, 2004; Furukawa & Ponce, 2009; Kumar et al., 2019; 2017). Accordingly, the SIDP problem generally boils down to an ambitious fitting problem, to which deep learning provides a suitable way to predict an acceptable solution to this problem (Yuan et al., 2022; Yin et al., 2019).

Impressive earlier methods use Markov Random Fields (MRF) to model monocular cues and the relation between several over-segmented image parts (Saxena et al., 2007; 2008). Nevertheless, with the recent surge in neural network architectures (Krizhevsky et al., 2012; Simonyan & Zisserman, 2015; He et al., 2016), which has an extraordinary capability to perform complex regression, many current works use deep learning to solve SIDP and have demonstrated high-quality results (Yuan et al., 2022; Aich et al., 2021; Bhat et al., 2021; Eigen et al., 2014; Fu et al., 2018; Lee et al., 2019;

*Corresponding Author
[1]kitti_depth_prediction_benchmark
[2]For official code refer here

2021). Popular recent methods for SIDP are mostly supervised. But even then, they are used less in real-world applications than geometric multiple view methods (Labbé & Michaud, 2019; Müller et al., 2022). Nonetheless, a good solution to SIDP is highly desirable in robotics (Yang et al., 2020), virtual-reality (Hoiem et al., 2005), augmented reality (Du et al., 2020), view synthesis (Hoiem et al., 2005) and other related vision tasks (Liu et al., 2019).

In this paper, we advocate that despite the supervised approach being encouraging, SIDP advancement should not wholly rely on the increase of dataset sizes. Instead, geometric cues and scene priors could help improve the SIDP results. Not that scene priors have not been studied to improve SIDP accuracy in the past. For instance, Chen et al. (2016) uses pairwise ordinal relations between points to learn scene depth. Alternatively, Yin et al. (2019) uses surface normals as an auxiliary loss to improve performance. Other heuristic approaches, such as Qi et al. (2018), jointly exploit the depth-to-normal relation to recover scene depth and surface normals. Yet, such state-of-the-art SIDP methods have limitations: for example, the approach in Chen et al. (2016) - using ordinal relation to learn depth - over-smooths the depth prediction results, thereby failing to preserve high-frequency surface details. Conversely, Yin et al. (2019) relies on good depth map prediction from a deep network and the idea of virtual normal. The latter is computed by randomly sampling three non-collinear points with large distances. This is rather complex and heuristic in nature. Qi et al. (2018) uses depth and normal consistency, which is good, yet it requires good depth map initialization.

This brings us to the point that further generalization of the regression-based SIDP pipeline is required. As mentioned before, existing approaches in this direction have limitations and are complex. In this paper, we propose a simple approach that provides better depth accuracy and generalizes well across different scenes. To this end, we resort to the physics of variation (Mollenhoff et al., 2016; Chambolle et al., 2010) in the neural network design for better generalization of the SIDP network, which by the way, keeps the essence of affine invariance (Yin et al., 2019). An image of a general scene—indoor or outdoor, has a lot of spatial regularity. And therefore, introducing a variational constraint provides a convenient way to ensure spatial regularity and to preserve information related to the scene discontinuities (Chambolle et al., 2010). Consequently, the proposed network is trained in a fully-supervised manner while encouraging the network to be mindful of the scene regularity where the variation in the depth gradient is large (cf. Sec.3.1). In simple terms, depth regression must be more than parameter fitting, and at some point, a mindful decision must be made—either by imaging features or by scene depth gradient variation, or both. As we demonstrate later in the paper, such an idea boosts the network's depth accuracy while preserving the high-frequency and low-frequency scene information (see Fig.1).

Our neural network for SIDP disentangles the absolute scale from the metric depth. It models an unscaled depth map as the optimal solution to the pixel-level variational constraints via weighted first-order differences, respecting the neighboring pixel depth gradients. Compared to previous methods, the network's task has been shifted away from pixel-wise metric depth learning to learning the first-order differences of the scene, which alleviates the scale ambiguity and favors scene regularity. To realize that, we initially employ a neural network to predict the first-order differences of the depth map. Then, we construct the partial differential equations representing the variational constraints by reorganizing the differences into a large matrix, i.e., an over-determined system of equations. Further, the network learns a weight matrix to eliminate redundant equations that do not favor the introduced first-order difference constraint. Finally, the closed-form depth map solution is recovered via simple matrix operations.

When tested on the KITTI (Geiger et al., 2012) and NYU Depth V2 (Silberman et al., 2012) test sets, our method outperforms prior art depth prediction accuracy by a large margin. Moreover, our model pre-trained on NYU Depth V2 better generalizes to the SUN RGB-D test set.

2 Prior Work

Depth estimation is a longstanding task in computer vision. In this work, we focus on a fully-supervised, single-image approach, and therefore, we discuss prior art that directly relates to such approach. Broadly, we divide the popular supervised SIDP methods into three sub-categories.

***(i)* Depth Learning using Ranking or Ordinal Relation Constraint.** Zoran et al. (2015) and Chen et al. (2016) argue that the ordinal relation between points is easier to learn than the metric depth. To this end, Zoran et al. (2015) proposes constrained quadratic optimization while Chen

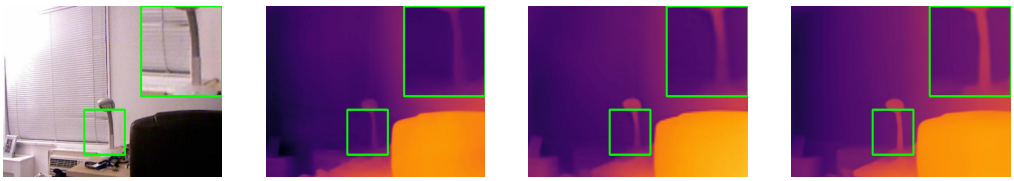

(a) Image (b) AdaBins (c) NeWCRFs (d) Ours

Figure 1: Qualitative comparison of our method's depth result with recent state-of-the-art methods such as AdaBins (Bhat et al., 2021), NeWCRFs (Yuan et al., 2022) on NYU Depth V2 test set (Silberman et al., 2012). It can be observed that our method predicts high-frequency details better than other recent methods.

et al. (2016) relies on the variation of the inception module to solve the problem. Later, Xian et al. (2020) proposes structure-guided sampling strategies for point pairs to improve training efficiency. Recently, Lienen et al. (2021) elaborates on the use of listwise ranking method based on the Plackett-Luce model (Luce, 2012). The drawback of such approaches is that the ordinal relationship and ranking over smooth the depth solution making accurate metric depth recovery challenging.

***(ii)* Depth Learning using Surface Normal Constraint.** Hu et al. (2019) introduces normal loss in addition to the depth loss to overcome the distorted and blurry edges in the depth prediction. Yin et al. (2019) proposes the concept of virtual normal to impose 3D scene constraint explicitly and to capture the long-range relations in the depth prediction. The long-range dependency in 3D is introduced via random sampling of three non-colinear points at a large distance from the virtual plane. Lately, Long et al. (2021) proposes an adaptive strategy to compute the local patch surface normals at train time from a set of randomly sampled candidates and overlooks it during test time.

***(iii)* Depth Learning using other Heuristic Refinement Constraint.** There has been numerous works attempt to refine the depth prediction as a post-processing step. Liu et al. (2015), Li et al. (2015) and Yuan et al. (2022) propose to utilize the Conditional Random Fields (CRF) to smooth the depth map. Lee et al. (2019) utilizes the planar assumptions to regularize the predicted depth map. Qi et al. (2018) adopts an auxiliary network to predict the surface normal, and then refine the predicted depth map following their proposed heuristic rules. There are mainly two problems with such approaches: Firstly, these approaches rely on a good depth map initialization. Secondly, the heuristic rules and the assumptions might result in over-smoothed depth values at objects boundaries.

Meanwhile, a few works, such as Ramamonjisoa et al. (2020), Cheng et al. (2018), Li et al. (2017) were proposed in the past with similar inspirations. Ramamonjisoa et al. (2020), Cheng et al. (2018) methods are generally motivated towards depth map refinement predicted from an off-the-shelf network. On the other hand, Cheng et al. (2018) proposes to use an affinity matrix that aims to learn the relation between each pixel's depth value and its neighbors' depth values. However, the affinity matrix has no explicit supervision, which could lead to imprecise learning of neighboring relations providing inferior results. On the contrary, our approach is mindful of imposing the first-order difference constraint leading to better performance. Earlier, Li et al. (2017) proposed two strategies for SIDP, i.e., fusion in an end-to-end network and fusion via optimization. The end-to-end strategy fuses the gradient and the depth map via convolution layers without any constraint on convolution weights, which may not be an apt choice for a depth regression problem such as SIDP. On the other hand, the fusion via optimization strategy is based on a non-differentiable strategy, leading to a non-end-to-end network loss function. Contrary to that, our method is well-constrained and performs quite well with a loss function that helps end-to-end learning of our proposed network. Not long ago, Lee & Kim (2019) proposed to estimate relative depths between pairs of images and ordinary depths at a different scale. By exploiting the rank-1 property of the pairwise comparison matrix, it recovers the relative depth map. Later, relative and ordinary depths are decomposed and fused to recover the depth. On a slightly different note, Lee & Kim (2020) studies the effectiveness of various losses and how to combine them for better monocular depth prediction.

To sum up, our approach allows learning of confidence weight to select reliable gradient estimation in a fully differentiable manner. Further, it proffers the benefits of the variational approach to overcome the limitations of the existing state-of-the-art methods. More importantly, the proposed method can provide excellent depth prediction without making extra assumptions such as good depth initialization, piece-wise planar scene, and assumptions used by previous works mentioned above.

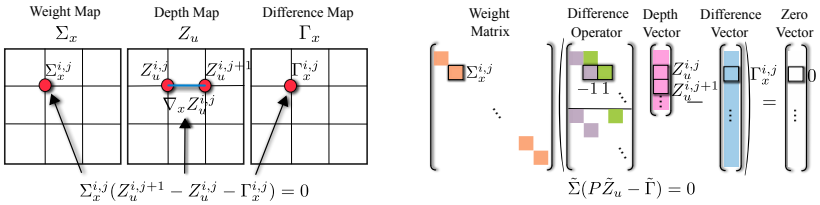

(a) First order depth variation along x-axis. (b) Overall matrix by ordering the terms.

Figure 2: **Illustration of the idea**. (a) Depth gradient constraint along x axis at location (i, j) in 4×4 matrix form. (b) Construction of the overall matrix formulation with constraints at all the pixel locations.

3 METHOD

In this section, we first describe our proposed variational constraint and then present the overall network architecture leading to the overall loss function.

3.1 VARIATIONAL CONSTRAINT

Here we introduce our variational constraint and how it can be useful for depth estimation. Consider an unscaled depth map as $Z_u \in \mathbb{R}^{H\times W}$, with (H, W) symbolizing the height and width, respectively. Assuming $\Gamma_x \in \mathbb{R}^{H\times W}$ and $\Gamma_y \in \mathbb{R}^{H\times W}$ as the gradient of Z_u in the x and y axis, we write

$$\nabla Z_u = [\Gamma_x,\ \Gamma_y]^{\mathrm{T}}. \tag{1}$$

Here, x and y subscript corresponds to the direction from left to right (x-axis) and top to bottom of the image (y-axis), respectively. Elaborating on this, we can write

$$\Gamma_x^{i,j} = \nabla_x Z_u^{i,j} = Z_u^{i,j+1} - Z_u^{i,j};\ \ \Gamma_y^{i,j} = \nabla_y Z_u^{i,j} = Z_u^{i+1,j} - Z_u^{i,j}. \tag{2}$$

Suppose we augment Eq.(2) expression for all (i, j), $i \in \{1, ..., H\}$ and $j \in \{1, ..., W\}$. In that case, we will end up with an over-determined system with $2HW$ equations in total. Given the predicted Γ_x and Γ_y, we aim to recover the HW unknown variables in Z_u. However, some of the equations could be spurious and deteriorate the overall depth estimation result rather than improving it. As a result, we must be mindful about selecting the equation that respects the imposed first-order constraint and maintains the depth gradient to have a meaningful fitting for better generalization. To that end, we introduce confidence weight $\Sigma_x \in [0, 1]^{H\times W}$, $\Sigma_y \in [0, 1]^{H\times W}$ for gradient along x, y direction. Consequently, we multiply the above two equations by the confidence weight term $\Sigma_x^{i,j}$ and $\Sigma_y^{i,j}$, respectively. On one hand, if the confidence is close to 1, the equation will have priority to be satisfied by the optimal Z_u. On the other hand, if the confidence is close to 0, we must ignore the equation. For better understanding, we illustrate the first-order difference and weighted matrix construction in Fig.2 (a) and Fig.2 (b).

Next, we reshape the Σ_x, Σ_y, Γ_x, Γ_y, and Z_u into column vectors $\tilde{\Sigma}_x \in [0, 1]^{HW\times 1}$, $\tilde{\Sigma}_y \in [0, 1]^{HW\times 1}$, $\tilde{\Gamma}_x \in \mathbb{R}^{HW\times 1}$, $\tilde{\Gamma}_y \in \mathbb{R}^{HW\times 1}$, and $\tilde{Z}_u \in \mathbb{R}^{HW\times 1}$, respectively. Organizing $\tilde{\Sigma} = \mathbf{diag}([\tilde{\Sigma}_x; \tilde{\Sigma}_y]) \in \mathbb{R}^{2HW\times 2HW}$ and $\tilde{\Gamma} = \mathbf{concat}[\tilde{\Gamma}_x; \tilde{\Gamma}_y] \in \mathbb{R}^{2HW\times 1}$, we can write the overall expression in a compact matrix form using simple algebra as follows

$$\tilde{\Sigma} P \tilde{Z}_u = \tilde{\Sigma}\tilde{\Gamma} \tag{3}$$

where $P \in \{1, -1\}^{2HW\times HW}$ is the first-order difference operator. Specifically, P is a sparse matrix with only a few elements as 1 or -1. The ith row of P provides the first-order difference operator for the ith equation. The position of 1 and -1 indicates which pair of neighbors to be considered for the constraint. Fig.2 (b) provides a visual intuition about this matrix equation.

Eq.(3) can be utilized to recover Z_u from the predicted Γ_x, Γ_y, Σ_x, and Σ_y. As alluded to above, we have more equations than unknowns, hence, we resort to recovering the optimal depth map

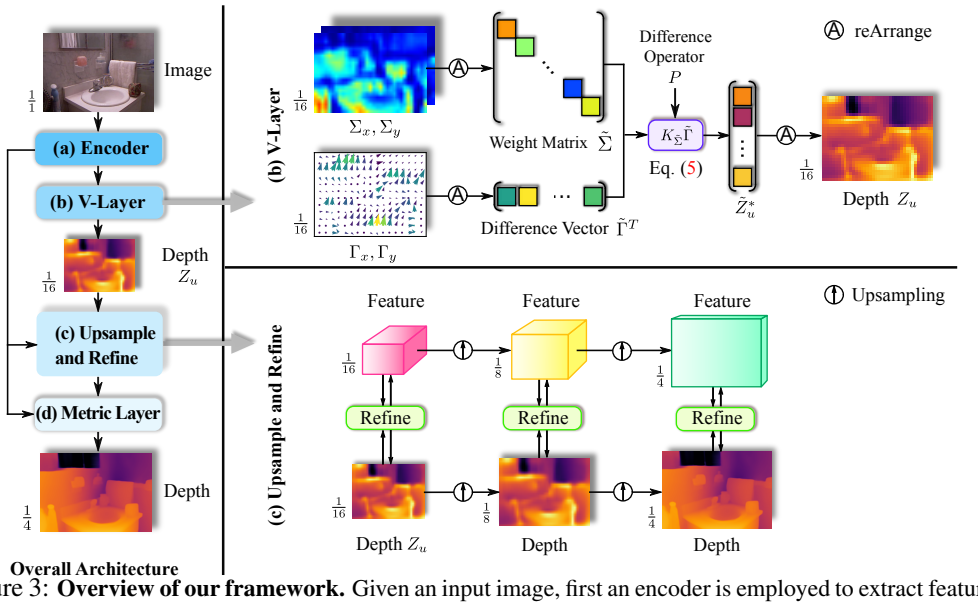

Figure 3: **Overview of our framework.** Given an input image, first an encoder is employed to extract features. Then we predict the depth map by the V-layer. Next, we gradually upsample and refine the depth map. In the end, we recover the metric depth by the metric layer.

$\tilde{Z}_u^* \in \mathbb{R}^{HW\times 1}$ by minimizing the following equation:

$$\tilde{Z}_u^* = \arg\min_{\tilde{Z}_u} ||\tilde{\Sigma}(P\tilde{Z}_u - \tilde{\Gamma})||_2. \tag{4}$$

Refer Appendix for the full derivation. The closed-form solution can be written as follows:

$$\tilde{Z}_u^* = \overbrace{(P^T\tilde{\Sigma}^2 P)^{-1}P^T\tilde{\Sigma}^2}^{K_{\tilde{\Sigma}}}\tilde{\Gamma}. \tag{5}$$

Denote $K_{\tilde{\Sigma}} \triangleq (P^T\tilde{\Sigma}^2 P)^{-1}P^T\tilde{\Sigma}^2$ in Eq.(5), we write overall equation as $\tilde{Z}_u^* = K_{\tilde{\Sigma}}\tilde{\Gamma}$. Next, we describe the overall network architecture.

3.2 Overall Network Architecture

Our overall network architecture is composed of four main modules as follows.

***(a)* Encoder.** Given an input image, the encoder computes the hierarchical feature maps through a series of stages. To be precise, our encoder has four stages. Each stage contains transformer blocks (Liu et al., 2021b). At the end of each stage, we collect the final feature map as the output of the encoder resulting in the encoded feature maps with strides 4, 8, 16, and 32, respectively. Our encoder module is inspired by Liu et al. (2021b), a recent state-of-the-art transformer network design. We use it as our backbone by removing the final global pooling layer and fully connected layer.

***(b)* Variational Layer (V-Layer).** The goal of this layer is to compute a map from encoded feature maps to unscaled depth map, which adheres to the first-order variational constraint. As of V-layer, we feed the feature maps of strides 16 and 32 as input which is the output of the encoder. Since these features are at different resolutions, we up-sample the feature map of stride 32 to stride 16 via bi-linear interpolation and concatenate to construct $I_\Phi \in \mathbb{R}^{C\times H\times W}$, where (H, W, C) symbolizing the height, width, and the number of channels, respectively. Note that H, W is not the same as the original resolution of the ground-truth depth and images. We use of two convolutional layers on I_Φ to predict the depth gradient and corresponding weight for each pixel as follows:

$$\{\Gamma_x, \Gamma_y, \Sigma_x, \Sigma_y\} = f(I_\Phi; \theta) \tag{6}$$

where, $f(I_\Phi; \theta)$ denotes the convolutional layers with parameters θ. The predicted depth gradients Γ_x and Γ_y are observed to be more accurate at smooth surface than at boundaries. This brings

us again to the point made above that we must take care of which first-order constraint must be included and discarded during regression. Using the Eq.(6) prediction, we construct the variational constraint Eq.(3), and obtain the unscaled depth map following Eq.(5). The resulting depth map has a resolution of 1/16 to the original image, which is later upsampled to the appropriate dimension.

To capture more scene features, we generate multiple channels (denoted as S) of $\{\Gamma_x, \Gamma_y, \Sigma_x, \Sigma_y\}$ using Eq.(6). As a result, we have a group of depth maps stacked along the channel dimension. For a feature map with spatial resolution $H \times W$, our V-layer has a complexity of $O(H^3W^3)$. To overcome complexity issue, we perform V-layer operation on feature maps with stride 16 and then up-sample and refine the depth maps in the later stage. The V-layer pipeline is shown in Fig.3(b).

***(c)* Upsample and Refine.** This module upsamples and refines the input depth map via encoded features at a given depth map resolution. To this end, we perform refinement at three different resolutions in a hierarchical manner. Given the V-layer depth map at 1/16 resolution, we first refine the depth via encoded features at this resolution. Concretely, this refinement is done using the following set of operations. (1) concatenate the feature map and the depth map; (2) use one convolutional layer with ReLU activation to fuse the feature and depth information; and (3) predict refined feature and depth map via a convolutional layer. Later, the refined feature and depth map are upsampled and fed into 1/8 for later refinement using the same above set of operations. Finally, the exact is done at 1/4 resolution. Note that these steps are performed in a sequel. At the end of this module, we have a depth map of 1/4 of the actual resolution. The upsample and refine procedure are shown in Fig.3(c).

***(d)* Metric Layer.** We must infer the global scene scale and shift to recover the metric depth. For this, we perform global max pooling on the encoded feature map of stride 32. The resulting vector is fed into a stack of fully connected layers to regress the two scalars, i.e., one representing the scale and while other representing the shift. Using the feature map of stride 32 is motivated by the observation that we have a much richer global scene context using it than at higher depth resolution. It also provides a good compromise between computational complexity and accuracy.

3.3 Loss Function

Depth Loss. It estimates the scale-invariant difference between the ground-truth depth and prediction at train time (Eigen et al., 2014). The difference is computed by upsampling the predicted depth map to the same resolution as the ground truth via bi-linear interpolation. Denoting the predicted and ground-truth depth as $\hat{Z} \in \mathbb{R}^{m \times n}$, $Z_{gt} \in \mathbb{R}^{m \times n}$ we compute the depth loss as follows

$$\mathcal{L}_{depth}(\hat{Z}, Z_{gt}) = \frac{1}{N}\sum_{(i,j)}(e^{i,j})^2 - \frac{\alpha}{N^2}(\sum_{i,j} e^{i,j})^2, \quad \text{where}, e^{i,j} = \log \hat{Z}^{i,j} - \log Z_{gt}^{i,j}. \tag{7}$$

Here, N is the number of positions with valid measurements and $\alpha \in [0, 1]$ is a hyper-parameter. Note that the above loss is used for valid measurements only.

Variational Loss. We define this loss using the output of V-layer. Suppose the ground-truth depth map to be $Z_{gt} \in \mathbb{R}^{m \times n}$ and the predicted depth map for S channels as $Z_u \in \mathbb{R}^{S \times H \times W}$. Since the depth resolution is not same at this layer, we downsample the ground truth. It is observed via empirical study that low-resolution depth map in fact help capture the first-order variational loss among distant neighbors. Accordingly, we downsample the Z_{gt} instead of upsamping Z_u. We downsample Z_{gt} denoted as $Q_{gt} \in \mathbb{R}^{H \times W}$ by random pooling operation, i.e., we randomly select a location where we have a valid measurement since ground-truth data may have pixels with no depth values. The coordinates of selected location in $Z_{gt} \mapsto Z_u \in \mathbb{R}^{S \times H \times W}$ and the corresponding depth value is put in $\hat{Q} \in \mathbb{R}^{S \times H \times W}$ via bi-linear interpolation. We compute the variational loss as

$$\mathcal{L}_{var}(\hat{Q}, Q_{gt}) = \frac{1}{N'}\sum_{(i,j)} |\text{Conv}(\hat{Q})^{i,j} - \nabla Q_{gt}^{i,j}| \tag{8}$$

where N' is the number of positions having valid measurements, ∇ symbolises the first-order difference operator, and Conv refers to the convolutional layer. Here, we use the Conv layer to fuse S depth maps into a single depth map and also to compute its horizontal and vertical gradient.

Total Loss. We define the total loss as the sum of the depth loss and the variational loss i.e., $\mathcal{L} = \mathcal{L}_{depth} + \lambda\mathcal{L}_{var}$, where λ is the regularization parameter set to 0.1 for all our experiments.

Table 1: Comparison with the state-of-the-art methods on the NYU test set (Silberman et al., 2012). Please refer to Sec.4.1 for details.

Method	Backbone	SILog ↓	Abs Rel ↓	RMS↓	RMS log↓	δ_1 ↑	δ_2 ↑
GeoNet (Qi et al., 2018)	ResNet-50	-	0.128	0.569	-	0.834	0.960
DORN (Fu et al., 2018)	ResNet-101	-	0.115	0.509	-	0.828	0.965
VNL (Yin et al., 2019)	ResNeXt-101	-	0.108	0.416	-	0.875	0.976
TransDepth (Yang et al., 2021)	ViT-B	-	0.106	0.365	-	0.900	0.983
ASN (Long et al., 2021)	HRNet-48	-	0.101	0.377	-	0.890	0.982
BTS (Lee et al., 2019)	DenseNet-161	11.533	0.110	0.392	0.142	0.885	0.978
DPT-Hybird (Ranftl et al., 2021)	ViT-B	-	0.110	0.357	-	0.904	0.988
AdaBins (Bhat et al., 2021)	EffNet-B5+ViT-mini	10.570	0.103	0.364	0.131	0.903	0.983
ASTrans (Chang et al., 2021)	ViT-B	10.429	0.103	0.374	0.132	0.902	0.985
NeWCRFs (Yuan et al., 2022)	Swin-L	9.102	0.095	0.331	0.119	0.922	**0.992**
Ours	Swin-L	**8.198**	**0.086**	**0.304**	**0.108**	**0.937**	**0.992**
% Improvement		-9.93%	-9.47%	-8.16%	-9.24%	+1.63%	+0.00%

Table 2: Comparison with the state-of-the-art methods on the the KITTI official test set (Geiger et al., 2012). We only list the results from the published methods. Please refer to Sec.4.1 for details.

Method	Backbone	SILog↓	Abs Rel↓	Sq Rel↓	iRMS↓
DLE (Liu et al., 2021a)	ResNet-34	11.81	9.09	2.22	12.49
DORN (Fu et al., 2018)	ResNet-101	11.80	8.93	2.19	13.22
BTS (Lee et al., 2019)	DenseNet-161	11.67	9.04	2.21	12.23
BANet (Aich et al., 2021)	DenseNet-161	11.55	9.34	2.31	12.17
PWA (Lee et al., 2021)	ResNeXt-101	11.45	9.05	2.30	12.32
ViP-DeepLab (Qiao et al., 2021)	-	10.80	8.94	2.19	11.77
NeWCRFs (Yuan et al., 2022)	Swin-L	10.39	8.37	1.83	11.03
Ours	Swin-L	**9.84**	**7.96**	**1.66**	**10.44**
% Improvement		-5.29%	-4.90%	-9.29%	-5.35%

4 Experiments and Results

Implementation Details We implemented our method in PyTorch 1.7.1 (Python 3.8) with CUDA 11.0. The software is evaluated on a computing machine with Quadro-RTX-6000 GPU.

Datasets. We performed experiments on three benchmark datasets namely NYU Depth V2 (Silberman et al., 2012), KITTI (Geiger et al., 2012), and SUN RGB-D (Song et al., 2015). ***(a)*** **NYU Depth V2** contains images with 480×640 resolution with depth values ranging from 0 to 10 meters. We follow the train and test set split from Lee et al. (2019), which contains 24,231 train images and 654 test images. ***(b)*** **KITTI** contains images with 352×1216 resolution where depth values range from 0 to 80 meters. The official split provides 42,949 train, 1,000 validation, and 500 test images. Eigen et al. (2014) provides another train and test set split for this dataset which has 23,488 train and 697 test images. ***(c)*** **SUN RGB-D** We preprocess its images to 480×640 resolution for consistency. The depth values range from 0 to 10 meters. We use the official test set (5050 images) for evaluation.

Training Details. We use (Liu et al., 2021b) network as our backbone, which is pre-trained on ImageNet (Deng et al., 2009). We use the Adam optimizer (Kingma & Ba, 2014) without weight decay. We decrease the learning rate from $3e^{-5}$ to $1e^{-5}$ by the cosine annealing scheduler. To avoid over-fitting, we augment the images by horizontal flipping. For KITTI (Geiger et al., 2012), the model is trained for 10 epochs for the official split and 20 epochs for the Eigen split (Eigen et al., 2014). For NYU Depth V2 (Silberman et al., 2012), the model is trained for 20 epochs.

Evaluation Metrics. We report statistical results on popular evaluation metrics such as square root of the Scale Invariant Logarithmic error (**SILog**), Relative Squared error (**Sq Rel**), Relative Absolute Error (**Abs Rel**), Root Mean Squared error (**RMS**), and threshold accuracy. Mathematical definition related to each one of them is provided in the Appendix.

4.1 Comparison to State of the Art

Tab.(1), Tab.(2), Tab.(3), and Tab.(4) provide statistical comparison results with the competing methods on NYU Depth V2, KITTI official split, KITTI Eigen split, and SUN RGB-D, respectively. Our proposed approach shows the best results for all the evaluation metrics. Particularly on the NYU test set, we reduce the SILog error from the previous best result, 9.102 to 8.198, and increase δ_1 from 0.922 to 0.937. More qualitative results including V-layer output are presented in the Appendix.

Table 3: Comparison with the state-of-the-art methods on the KITTI Eigen test set (Eigen et al., 2014).

Method	Backbone	SILog ↓	Abs Rel ↓	RMS↓	RMS log↓	δ_1 ↑	δ_2 ↑
DORN (Fu et al., 2018)	ResNet-101	-	0.072	0.273	0.120	0.932	0.984
VNL (Yin et al., 2019)	ResNeXt-101	-	0.072	0.326	0.117	0.938	0.990
TransDepth (Yang et al., 2021)	ViT-B	8.930	0.064	0.275	0.098	0.956	0.994
BTS (Lee et al., 2019)	DenseNet-161	8.933	0.060	0.280	0.096	0.955	0.993
DPT-Hybird (Ranftl et al., 2021)	ViT-B	-	0.062	0.257	-	0.959	0.995
AdaBins (Bhat et al., 2021)	EffNet-B5+ViT-mini	8.022	0.058	0.236	0.089	0.964	0.995
ASTrans (Chang et al., 2021)	ViT-B	7.897	0.058	0.269	0.089	0.963	0.995
NeWCRFs (Yuan et al., 2022)	Swin-L	6.986	0.052	0.213	0.079	0.974	**0.997**
Ours	Swin-L	**6.817**	**0.050**	**0.209**	**0.076**	**0.977**	**0.997**
% Improvement		-2.42%	-3.85%	-1.88%	-3.80%	+0.03%	+0.00%

Table 4: Comparison with AdaBins and NeWCRFs on SUN RGB-D test set. All methods are trained on NYU Depth V2 train set without fine-tuning on SUN RGB-D.

Method	Backbone	SILog ↓	Abs Rel ↓	RMS↓	RMS log↓	δ_1 ↑	δ_2 ↑
AdaBins(Bhat et al., 2021)	EffNet-B5+ViT-mini	13.652	0.110	0.321	0.137	0.906	0.982
NeWCRFs (Yuan et al., 2022)	Swin-L	13.695	0.105	0.322	0.138	0.920	0.980
Ours	Swin-L	**12.596**	**0.094**	**0.299**	**0.127**	**0.929**	**0.983**
% Improvement		-7.73%	-10.48%	-6.85%	-7.30%	+0.98%	+0.10%

For the SUN RGB-D test set, all competing models, including ours, are trained on the NYU Depth V2 training set (Silberman et al., 2012) *without* fine-tuning on the SUN RGB-D. In addition, we align the predictions from all the models with the ground truth by a scale and shift following Ranftl et al. (2020). Tab.(4) results show our method's better generalization capability than other approaches. Extensive visual results are provided in the Appendix and supplementary video.

4.2 Ablation Study

All the ablation presented below is conducted on NYU Depth V2 test set (Silberman et al., 2012).

***(i)* Effect of V-Layer.** To understand the benefit and outcome of our variational layer compared to other popular alternative layers in deep neural networks for this problem, we performed this ablation study. We replace our V-layer firstly with a convolutional layer and later with a self-attention layer. Tab.(5) provides the depth prediction accuracy for this ablation. For each introduced layer in Tab.(5), the first and second rows show the performance of the depth map predicted *with* (w) and *without* (w/o) subsequent refinements (cf. Sec.3.2 (c)), respectively. For the self-attention layer, we follow the ViT (Dosovitskiy et al., 2021) and set the patch size to be one as we use the feature map with stride 16. We also adopt the learnable position embedding (PE) with 128 dimensions. We set the number of heads to be 4 and the number of hidden units to be 512. As shown in Tab.(5), our V-layer indeed helps improve the accuracy of depth prediction compared to other well-known layers. More experiments on KITTI and SUN RBG-D are provided in the Appendix.

***(ii)* Performance with Different Network Backbone.** We evaluate the effects of our V-layer with different types of network backbones. For this ablation, we use Swin-Large (Liu et al., 2021b), Swin-Small (Liu et al., 2021b), and ConvNeXt-Small (Liu et al., 2022). The SILog error is shown in Fig. 4. The results show that our V-layer improves the transformer and the convolutional network performance. An important observation is that our V-layer shows excellent improvements in depth prediction accuracy on weaker network backbones.

***(iii)* Performance with Change in the Value of S.** For this ablation, we change the value of S in the V-layer and observe its effects (cf. Sec.3.2 (b)). By increasing S, we generate more channels of $\tilde{\Gamma}$ and $\tilde{\Sigma}$ which in-effect increases V-layer parameters. In the subsequent step, we expand the

Table 5: **Benefit of V-layer.** We replace the proposed V-layer with a single convolutional layer and a self-attention layer, and evaluate the accuracy of depth map predicted with and without subsequent refinements.

Layer	Refine	SILog ↓	Abs Rel ↓	RMS↓	RMS log ↓	δ_1 ↑	δ_2 ↑
Convolution	w/o	8.830	0.090	0.325	0.114	0.927	0.990
	w/	8.688	0.089	0.317	0.113	0.928	0.991
Self-Attention + PE	w/o	8.790	0.090	0.318	0.114	0.927	0.990
	w/	8.595	0.089	0.316	0.112	0.929	0.991
V-Layer	w/o	8.422	0.087	0.308	0.110	0.936	0.990
	w/	**8.198**	**0.086**	**0.304**	**0.108**	**0.937**	**0.992**

number of channels to 128 by a convolutional layer to use the subsequent layers as they are. The results are shown in Tab.(6). For reference, we also present the result by replacing the V-layer with a convolutional layer in the first row in Tab.(6). By increasing S, we reduce the SILog error, at the price of the speed (FPS). Yet, no real benefit is observed with S more than 16.

***(iv)* Effect of Confidence Weight Matrix & Difference Operator in V-Layer.** For this ablation, we study the network's depth prediction under four different settings. (a) without V-layer and replace it with convolutional layer (b) without the confidence weight matrix (c) with learnable difference operator and (d) our full model. The depth prediction accuracy observed under these settings is provided in Tab.(7). Clearly, our full model has better accuracy. An important empirical observation, we made during this test is when we keep P learnable V-layer has more learnable parameters, the performance becomes worse than with fixed difference operator.

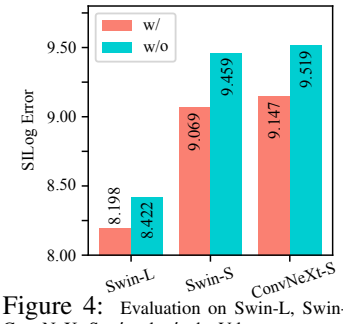

Figure 4: Evaluation on Swin-L, Swin-S, ConvNeXt-S **w/** and **w/o** the V-layer.

Table 6: Analysis of the number of feature groups. More groups reduce the SILog error.

	SILog↓	Abs Rel↓	RMS↓	FPS ↑
w/o V-layer	8.688	0.089	0.317	**9.343**
1	8.456	0.088	0.310	8.175
16	8.198	0.086	**0.304**	7.032
128	**8.172**	**0.085**	0.309	3.320

Table 7: Analysis of the confidence weight matrix $\tilde{\Sigma}$ and the difference operator P.

	SILog↓	Abs Rel↓	RMS ↓
(a) w/o V-layer	8.688	0.089	0.317
(b) w/o $\tilde{\Sigma}$	8.537	0.089	0.316
(c) learnable P	8.355	0.088	0.310
(d) **full**	**8.198**	**0.086**	**0.304**

4.3 Network processing time & Parameters

We compared our method's inference time and the number of model parameters to the AdaBins (Bhat et al., 2021) and the NeWCRFs (Yuan et al., 2022). The inference time is measured on the NYU Depth V2 test set with batch size 1. We have removed the ensemble tricks in AdaBins and NeWCRFs for an unbiased evaluation, resulting in a slight increase in SILog error as compared to Tab.(1) statistics. As is shown in Tab.(8), our method is faster and better than AdaBins and NeWCRFs using Swin-Small backbone. With the same backbone as the NeWCRFs, i.e., Swin-Large, we achieve much better depth prediction results. Hence, our method with Swin-Small backbone provides a better balance between accuracy, speed and memory foot-print.

Table 8: Comparison of the inference time and parameters to AdaBins and NeWCRFs on NYU Depth V2. We show our results using the Swin-Small and Swin-Large backbone.

	AdaBins (Bhat et al., 2021)	NeWCRFs (Yuan et al., 2022)	Ours (Small)	Ours (Large)
SILog Error ↓	10.651	9.171	**9.069**	**8.198**
Speed (FPS) ↑	5.638	10.551	**11.891**	7.032
Param (M) ↓	**75**	258	**76**	249

5 Conclusion

In conclusion, a simple and effective approach for inferring scene depth from a single image is introduced. The proposed SIDP approach is shown to better exploit the rigid scene prior, which is generally overlooked by the existing neural network-based methods. Our approach does not make explicit assumptions about the scene other than the scene gradient regularity, which holds for typical indoor or outdoor scenes. When tested on popular benchmark datasets, our method shows significantly better results than the prior art, both qualitatively and quantitatively.

6 Acknowledgment

This work was partly supported by ETH General Fund (OK), Chinese Scholarship Council (CSC), and The Alexander von Humboldt Foundation.

REFERENCES

Shubhra Aich, Jean Marie Uwabeza Vianney, Md Amirul Islam, and Mannat Kaur Bingbing Liu. Bidirectional attention network for monocular depth estimation. In *2021 IEEE International Conference on Robotics and Automation (ICRA)*, pp. 11746–11752. IEEE, 2021.

Shariq Farooq Bhat, Ibraheem Alhashim, and Peter Wonka. Adabins: Depth estimation using adaptive bins. In *Proceedings of the IEEE/CVF Conference on Computer Vision and Pattern Recognition*, pp. 4009–4018, 2021.

Antonin Chambolle, Vicent Caselles, Daniel Cremers, Matteo Novaga, and Thomas Pock. An introduction to total variation for image analysis. *Theoretical foundations and numerical methods for sparse recovery*, 9(263-340):227, 2010.

Wenjie Chang, Yueyi Zhang, and Zhiwei Xiong. Transformer-based monocular depth estimation with attention supervision. In *32nd British Machine Vision Conference (BMVC 2021)*, 2021.

Weifeng Chen, Zhao Fu, Dawei Yang, and Jia Deng. Single-image depth perception in the wild. *Advances in neural information processing systems*, 29, 2016.

Xinjing Cheng, Peng Wang, and Ruigang Yang. Depth estimation via affinity learned with convolutional spatial propagation network. In *Proceedings of the European Conference on Computer Vision (ECCV)*, pp. 103–119, 2018.

Jia Deng, Wei Dong, Richard Socher, Li-Jia Li, Kai Li, and Li Fei-Fei. Imagenet: A large-scale hierarchical image database. In *2009 IEEE conference on computer vision and pattern recognition*, pp. 248–255. Ieee, 2009.

Alexey Dosovitskiy, Lucas Beyer, Alexander Kolesnikov, Dirk Weissenborn, Xiaohua Zhai, Thomas Unterthiner, Mostafa Dehghani, Matthias Minderer, Georg Heigold, Sylvain Gelly, Jakob Uszkoreit, and Neil Houlsby. An image is worth 16x16 words: Transformers for image recognition at scale. In *International Conference on Learning Representations*, 2021.

Ruofei Du, Eric Turner, Maksym Dzitsiuk, Luca Prasso, Ivo Duarte, Jason Dourgarian, Joao Afonso, Jose Pascoal, Josh Gladstone, Nuno Cruces, et al. Depthlab: Real-time 3d interaction with depth maps for mobile augmented reality. In *Proceedings of the 33rd Annual ACM Symposium on User Interface Software and Technology*, pp. 829–843, 2020.

David Eigen, Christian Puhrsch, and Rob Fergus. Depth map prediction from a single image using a multi-scale deep network. *Advances in neural information processing systems*, 27, 2014.

Huan Fu, Mingming Gong, Chaohui Wang, Kayhan Batmanghelich, and Dacheng Tao. Deep ordinal regression network for monocular depth estimation. In *Proceedings of the IEEE conference on computer vision and pattern recognition*, pp. 2002–2011, 2018.

Yasutaka Furukawa and Jean Ponce. Accurate, dense, and robust multiview stereopsis. *IEEE transactions on pattern analysis and machine intelligence*, 32(8):1362–1376, 2009.

Andreas Geiger, Philip Lenz, and Raquel Urtasun. Are we ready for autonomous driving? the kitti vision benchmark suite. In *2012 IEEE conference on computer vision and pattern recognition*, pp. 3354–3361. IEEE, 2012.

Kaiming He, Xiangyu Zhang, Shaoqing Ren, and Jian Sun. Deep residual learning for image recognition. In *Proceedings of the IEEE conference on computer vision and pattern recognition*, pp. 770–778, 2016.

Derek Hoiem, Alexei A Efros, and Martial Hebert. Automatic photo pop-up. In *ACM SIGGRAPH 2005 Papers*, pp. 577–584. Association for Computing Machinery, 2005.

Junjie Hu, Mete Ozay, Yan Zhang, and Takayuki Okatani. Revisiting single image depth estimation: Toward higher resolution maps with accurate object boundaries. In *2019 IEEE Winter Conference on Applications of Computer Vision (WACV)*, pp. 1043–1051. IEEE, 2019.

Po-Han Huang, Kevin Matzen, Johannes Kopf, Narendra Ahuja, and Jia-Bin Huang. Deepmvs: Learning multi-view stereopsis. In *Proceedings of the IEEE Conference on Computer Vision and Pattern Recognition*, pp. 2821–2830, 2018.

Berk Kaya, Suryansh Kumar, Carlos Oliveira, Vittorio Ferrari, and Luc Van Gool. Uncertainty-aware deep multi-view photometric stereo. In *Proceedings of the IEEE/CVF Conference on Computer Vision and Pattern Recognition*, pp. 12601–12611, 2022.

Diederik P Kingma and Jimmy Ba. Adam: A method for stochastic optimization. *arXiv preprint arXiv:1412.6980*, 2014.

Alex Krizhevsky, Ilya Sutskever, and Geoffrey E Hinton. Imagenet classification with deep convolutional neural networks. *Advances in neural information processing systems*, 25, 2012.

Suryansh Kumar, Yuchao Dai, and Hongdong Li. Monocular dense 3d reconstruction of a complex dynamic scene from two perspective frames. In *Proceedings of the IEEE international conference on computer vision (ICCV)*, pp. 4649–4657, 2017.

Suryansh Kumar, Yuchao Dai, and Hongdong Li. Superpixel soup: Monocular dense 3d reconstruction of a complex dynamic scene. *IEEE transactions on pattern analysis and machine intelligence (TPAMI)*, 43(5):1705–1717, 2019.

Mathieu Labbé and François Michaud. Rtab-map as an open-source lidar and visual simultaneous localization and mapping library for large-scale and long-term online operation. *Journal of Field Robotics*, 36(2):416–446, 2019.

Jae-Han Lee and Chang-Su Kim. Monocular depth estimation using relative depth maps. In *Proceedings of the IEEE/CVF Conference on Computer Vision and Pattern Recognition*, pp. 9729–9738, 2019.

Jae-Han Lee and Chang-Su Kim. Multi-loss rebalancing algorithm for monocular depth estimation. In *European Conference on Computer Vision*, pp. 785–801. Springer, 2020.

Jin Han Lee, Myung-Kyu Han, Dong Wook Ko, and Il Hong Suh. From big to small: Multi-scale local planar guidance for monocular depth estimation. *arXiv preprint arXiv:1907.10326*, 2019.

Sihaeng Lee, Janghyeon Lee, Byungju Kim, Eojindl Yi, and Junmo Kim. Patch-wise attention network for monocular depth estimation. In *Proceedings of the AAAI Conference on Artificial Intelligence*, volume 35, pp. 1873–1881, 2021.

Bo Li, Chunhua Shen, Yuchao Dai, Anton van den Hengel, and Mingyi He. Depth and surface normal estimation from monocular images using regression on deep features and hierarchical crfs. In *Proceedings of the IEEE Conference on Computer Vision and Pattern Recognition (CVPR)*, June 2015.

Jun Li, Reinhard Klein, and Angela Yao. A two-streamed network for estimating fine-scaled depth maps from single rgb images. In *Proceedings of the IEEE International Conference on Computer Vision*, pp. 3372–3380, 2017.

Julian Lienen, Eyke Hüllermeier, Ralph Ewerth, and Nils Nommensen. Monocular depth estimation via listwise ranking using the plackett-luce model. In *Proceedings of the IEEE/CVF Conference on Computer Vision and Pattern Recognition (CVPR)*, pp. 14595–14604, June 2021.

Ce Liu, Shuhang Gu, Luc Van Gool, and Radu Timofte. Deep line encoding for monocular 3d object detection and depth prediction. In *32nd British Machine Vision Conference (BMVC 2021)*, pp. 354, 2021a.

Fayao Liu, Chunhua Shen, Guosheng Lin, and Ian Reid. Learning depth from single monocular images using deep convolutional neural fields. *IEEE transactions on pattern analysis and machine intelligence*, 38(10):2024–2039, 2015.

Xingtong Liu, Ayushi Sinha, Masaru Ishii, Gregory D Hager, Austin Reiter, Russell H Taylor, and Mathias Unberath. Dense depth estimation in monocular endoscopy with self-supervised learning methods. *IEEE transactions on medical imaging*, 39(5):1438–1447, 2019.

Ze Liu, Yutong Lin, Yue Cao, Han Hu, Yixuan Wei, Zheng Zhang, Stephen Lin, and Baining Guo. Swin transformer: Hierarchical vision transformer using shifted windows. In *Proceedings of the IEEE/CVF International Conference on Computer Vision*, pp. 10012–10022, 2021b.

Zhuang Liu, Hanzi Mao, Chao-Yuan Wu, Christoph Feichtenhofer, Trevor Darrell, and Saining Xie. A convnet for the 2020s. In *Proceedings of the IEEE/CVF Conference on Computer Vision and Pattern Recognition*, pp. 11976–11986, 2022.

Xiaoxiao Long, Cheng Lin, Lingjie Liu, Wei Li, Christian Theobalt, Ruigang Yang, and Wenping Wang. Adaptive surface normal constraint for depth estimation. In *Proceedings of the IEEE/CVF International Conference on Computer Vision*, pp. 12849–12858, 2021.

H Christopher Longuet-Higgins. A computer algorithm for reconstructing a scene from two projections. *Nature*, 293(5828):133–135, 1981.

R Duncan Luce. *Individual choice behavior: A theoretical analysis*. Courier Corporation, 2012.

Ben Mildenhall, Pratul P Srinivasan, Matthew Tancik, Jonathan T Barron, Ravi Ramamoorthi, and Ren Ng. Nerf: Representing scenes as neural radiance fields for view synthesis. *Communications of the ACM*, 65(1):99–106, 2021.

Thomas Mollenhoff, Emanuel Laude, Michael Moeller, Jan Lellmann, and Daniel Cremers. Sublabel-accurate relaxation of nonconvex energies. In *Proceedings of the IEEE Conference on Computer Vision and Pattern Recognition*, pp. 3948–3956, 2016.

Thomas Müller, Alex Evans, Christoph Schied, and Alexander Keller. Instant neural graphics primitives with a multiresolution hash encoding. *ACM Trans. Graph.*, 41(4):102:1–102:15, July 2022. doi: 10.1145/3528223.3530127.

David Nistér. An efficient solution to the five-point relative pose problem. *IEEE transactions on pattern analysis and machine intelligence*, 26(6):756–770, 2004.

Adam Paszke, Sam Gross, Francisco Massa, Adam Lerer, James Bradbury, Gregory Chanan, Trevor Killeen, Zeming Lin, Natalia Gimelshein, Luca Antiga, et al. Pytorch: An imperative style, high-performance deep learning library. *Advances in neural information processing systems*, 32, 2019.

Xiaojuan Qi, Renjie Liao, Zhengzhe Liu, Raquel Urtasun, and Jiaya Jia. Geonet: Geometric neural network for joint depth and surface normal estimation. In *Proceedings of the IEEE Conference on Computer Vision and Pattern Recognition*, pp. 283–291, 2018.

Siyuan Qiao, Yukun Zhu, Hartwig Adam, Alan Yuille, and Liang-Chieh Chen. Vip-deeplab: Learning visual perception with depth-aware video panoptic segmentation. In *Proceedings of the IEEE/CVF Conference on Computer Vision and Pattern Recognition*, pp. 3997–4008, 2021.

Michael Ramamonjisoa, Yuming Du, and Vincent Lepetit. Predicting sharp and accurate occlusion boundaries in monocular depth estimation using displacement fields. In *Proceedings of the IEEE/CVF Conference on Computer Vision and Pattern Recognition*, pp. 14648–14657, 2020.

René Ranftl, Katrin Lasinger, David Hafner, Konrad Schindler, and Vladlen Koltun. Towards robust monocular depth estimation: Mixing datasets for zero-shot cross-dataset transfer. *IEEE Transactions on Pattern Analysis and Machine Intelligence (TPAMI)*, 2020.

René Ranftl, Alexey Bochkovskiy, and Vladlen Koltun. Vision transformers for dense prediction. In *Proceedings of the IEEE/CVF International Conference on Computer Vision*, pp. 12179–12188, 2021.

Ashutosh Saxena, Min Sun, and Andrew Y Ng. Learning 3d scene structure from a single still image. In *2007 IEEE 11th international conference on computer vision*, pp. 1–8. IEEE, 2007.

Ashutosh Saxena, Min Sun, and Andrew Y Ng. Make3d: Learning 3d scene structure from a single still image. *IEEE transactions on pattern analysis and machine intelligence*, 31(5):824–840, 2008.

Nathan Silberman, Derek Hoiem, Pushmeet Kohli, and Rob Fergus. Indoor segmentation and support inference from rgbd images. In *European conference on computer vision*, pp. 746–760. Springer, 2012.

Karen Simonyan and Andrew Zisserman. Very deep convolutional networks for large-scale image recognition. In *International Conference on Learning Representations*, 2015.

Shuran Song, Samuel P Lichtenberg, and Jianxiong Xiao. Sun rgb-d: A rgb-d scene understanding benchmark suite. In *Proceedings of the IEEE conference on computer vision and pattern recognition*, pp. 567–576, 2015.

Zachary Teed and Jia Deng. Droid-slam: Deep visual slam for monocular, stereo, and rgb-d cameras. *Advances in Neural Information Processing Systems*, 34:16558–16569, 2021.

Dmitry Ulyanov, Andrea Vedaldi, and Victor Lempitsky. Instance normalization: The missing ingredient for fast stylization. *arXiv preprint arXiv:1607.08022*, 2016.

Ashish Vaswani, Noam Shazeer, Niki Parmar, Jakob Uszkoreit, Llion Jones, Aidan N Gomez, Łukasz Kaiser, and Illia Polosukhin. Attention is all you need. *Advances in neural information processing systems*, 30, 2017.

Ke Xian, Jianming Zhang, Oliver Wang, Long Mai, Zhe Lin, and Zhiguo Cao. Structure-guided ranking loss for single image depth prediction. In *Proceedings of the IEEE/CVF Conference on Computer Vision and Pattern Recognition*, pp. 611–620, 2020.

Guanglei Yang, Hao Tang, Mingli Ding, Nicu Sebe, and Elisa Ricci. Transformer-based attention networks for continuous pixel-wise prediction. In *Proceedings of the IEEE/CVF International Conference on Computer Vision*, pp. 16269–16279, 2021.

Nan Yang, Lukas von Stumberg, Rui Wang, and Daniel Cremers. D3vo: Deep depth, deep pose and deep uncertainty for monocular visual odometry. In *Proceedings of the IEEE/CVF conference on computer vision and pattern recognition*, pp. 1281–1292, 2020.

Wei Yin, Yifan Liu, Chunhua Shen, and Youliang Yan. Enforcing geometric constraints of virtual normal for depth prediction. In *Proceedings of the IEEE/CVF International Conference on Computer Vision*, pp. 5684–5693, 2019.

Weihao Yuan, Xiaodong Gu, Zuozhuo Dai, Siyu Zhu, and Ping Tan. Neural window fully-connected crfs for monocular depth estimation. In *Proceedings of the IEEE/CVF Conference on Computer Vision and Pattern Recognition (CVPR)*, pp. 3916–3925, June 2022.

Daniel Zoran, Phillip Isola, Dilip Krishnan, and William T Freeman. Learning ordinal relationships for mid-level vision. In *Proceedings of the IEEE international conference on computer vision*, pp. 388–396, 2015.

A Appendix

A.1 Training Details

We implement our framework in PyTorch (Paszke et al., 2019). We adopt the Swin-Large (Liu et al., 2021b) as our backbone to conduct ablation experiments and compare with the state of the arts. And the backbone is pre-trained on ImageNet-22K (Deng et al., 2009) by image classification. For training, we use the Adam optimizer (Kingma & Ba, 2014) without weight decay. We decrease the learning rate from $3e^{-5}$ to $1e^{-5}$ by the cosine annealing scheduler. To avoid over-fitting, we augment the images by horizontal flipping. For both train and test, we keep the resolution of images to be 352×1216 in KITTI (Geiger et al., 2012), and 480×640 in both NYU Depth V2 (Silberman et al., 2012) and SUN RGB-D (Song et al., 2015). In KITTI, the model is trained for 10 epochs for the official split and 20 epochs for the Eigen split (Eigen et al., 2014). In NYU Depth V2, the model is trained for 20 epochs. We set the batch size to be 4 and 8 respectively for ablation experiments and comparison to the state of the arts.

A.2 Evaluation Metrics

Suppose the predicted and ground-truth depth to be $\hat{Z} \in \mathbb{R}^{m \times n}$ and $Z_{gt} \in \mathbb{R}^{m \times n}$, respectively, and the number of valid pixels to be N. We follow the existing methods (Yuan et al., 2022) and utilize the following measures for quantitative evaluation:

- square root of the Scale Invariant Logarithmic error (**SILog**): $\frac{1}{N}\sum_{i,j}(e^{i,j})^2 - \frac{1}{N^2}(\sum_{i,j} e^{i,j})^2$, where $e^{i,j} = \log \hat{Z}^{i,j} - \log Z_{gt}^{i,j}$;
- Relative Squared error (**Sq Rel**): $\frac{1}{N}\sum_{i,j}(\hat{Z}^{i,j} - Z_{gt}^{i,j})^2 / Z_{gt}^{i,j}$;
- Relative Absolute Error (**Abs Rel**): $\frac{1}{N}\sum_{i,j}|\hat{Z}^{i,j} - Z_{gt}^{i,j}| / Z_{gt}^{i,j}$;
- Root Mean Squared error (**RMS**): $\frac{1}{N}\sqrt{\sum_{i,j}(\hat{Z}^{i,j} - Z_{gt}^{i,j})^2}$;
- Root Mean Squared Logarithmic error (**RMS log**): $\frac{1}{N}\sqrt{\sum_{i,j}(e^{i,j})^2}$;
- threshold accuracy ($\boldsymbol{\delta_k}$): percentage of $\hat{Z}^{i,j}$ s.t. $\max(\frac{\hat{Z}^{i,j}}{Z_{gt}^{i,j}}, \frac{Z_{gt}^{i,j}}{\hat{Z}^{i,j}}) < 1.25^k$.

A.3 Derivation of the Variational Constraint

In this part, we introduce the derivation of the variational constraint in more detail. Firstly, we present the detailed form of the difference operator P, the confidence weight matrix $\tilde{\Sigma}$, the difference vector $\tilde{\Gamma}$ and the depth vector $\tilde{Z}_u$, when the depth map Z_u is at resolution 2×2. Secondly we show the derivation of the optimal solution $\tilde{Z}_u^*$.

Overall Matrix Form. Suppose the unscaled depth map to be $Z_u \in \mathbb{R}^{2\times 2}$, the difference map to be $\Gamma_x \in \mathbb{R}^{2\times 2}$ and $\Gamma_y \in \mathbb{R}^{2\times 2}$, and the corresponding confidence weight map to be $\Sigma_x \in [0,1]^{2\times 2}$ and $\Sigma_y \in [0,1]^{2\times 2}$. We first reorganize the elements in Γ_x, Γ_y, Σ_x, Σ_y to construct the difference vector $\tilde{\Gamma} \in \mathbb{R}^{8\times 1}$ and the confidence weight matrix $\tilde{\Sigma} \in \mathbb{R}^{8\times 8}$:

$$\tilde{\Gamma} = \begin{pmatrix} \Gamma_x^{1,1} \\ \Gamma_x^{1,2} \\ \Gamma_x^{2,1} \\ \Gamma_x^{2,2} \\ \Gamma_y^{1,1} \\ \Gamma_y^{1,2} \\ \Gamma_y^{2,1} \\ \Gamma_y^{2,2} \end{pmatrix}, \tilde{\Sigma} = \begin{pmatrix} \Sigma_x^{1,1} & 0 & 0 & 0 & 0 & 0 & 0 & 0 \\ 0 & \Sigma_x^{1,2} & 0 & 0 & 0 & 0 & 0 & 0 \\ 0 & 0 & \Sigma_x^{2,1} & 0 & 0 & 0 & 0 & 0 \\ 0 & 0 & 0 & \Sigma_x^{2,2} & 0 & 0 & 0 & 0 \\ 0 & 0 & 0 & 0 & \Sigma_y^{1,1} & 0 & 0 & 0 \\ 0 & 0 & 0 & 0 & 0 & \Sigma_y^{1,2} & 0 & 0 \\ 0 & 0 & 0 & 0 & 0 & 0 & \Sigma_y^{2,1} & 0 \\ 0 & 0 & 0 & 0 & 0 & 0 & 0 & \Sigma_y^{2,2} \end{pmatrix}.$$

Next, we apply the difference operator $P \in \mathbb{R}^{8\times 4}$:

$$P = \begin{pmatrix} -1 & 1 & 0 & 0 \\ 0 & 0 & 0 & 0 \\ 0 & 0 & -1 & 1 \\ 0 & 0 & 0 & 1 \\ -1 & 0 & 1 & 0 \\ 0 & -1 & 0 & 1 \\ 0 & 0 & 0 & 0 \\ 0 & 0 & 0 & 1 \end{pmatrix}$$

on the depth vector $\tilde{Z}_u \in \mathbb{R}^{4\times 1}$:

$$\tilde{Z}_u = \begin{pmatrix} Z_u^{1,1} \\ Z_u^{1,2} \\ Z_u^{2,1} \\ Z_u^{2,2} \end{pmatrix}.$$

Finally, we construct the following constraint equation:

$$\tilde{\Sigma} P \tilde{Z}_u = \tilde{\Sigma}\tilde{\Gamma}. \tag{9}$$

In the above equation, each row represents a weighted constraint for the first-order difference along the x-axis:

$$\Sigma_x^{i,j}(Z_u^{i,j+1} - Z_u^{i,j}) = \Sigma_x^{i,j}\Gamma_x^{i,j} \tag{10}$$

or along the y-axis:

$$\Sigma_y^{i,j}(Z_u^{i+1,j} - Z_u^{i,j}) = \Sigma_y^{i,j}\Gamma_y^{i,j} \tag{11}$$

where $(Z_u^{i,j+1} - Z_u^{i,j}) = \Gamma_x^{i,j}$ and $(Z_u^{i+1,j} - Z_u^{i,j}) = \Gamma_y^{i,j}$ are the variational constraints for the first-order difference, while $\Sigma_x^{i,j}$ and $\Sigma_y^{i,j}$ are the confidence weights for the constraints.

Optimal Solution. Given $\tilde{\Sigma}$ and $\tilde{\Gamma}$, we search for the optimal depth vector $\tilde{Z}_u^*$ by minimizing the residual of Eq.(9):

$$\tilde{Z}_u^* = \arg\min_{\tilde{Z}_u} ||\tilde{\Sigma}(P\tilde{Z}_u - \tilde{\Gamma})||_2. \tag{12}$$

Firstly, the objective function, $||\tilde{\Sigma}(P\tilde{Z}_u - \tilde{\Gamma})||_2$, is convex with respect to $\tilde{Z}_u$. Because $||\cdot||_2$ is a convex function. A composition of $||\cdot||_2$ and the affine function , $\tilde{\Sigma}(P\tilde{Z}_u - \tilde{\Gamma})$, is still convex.

Secondly, the optimal solution of a convex function can be found at where the first derivative is zero. Thereby we obtain the final solution $\tilde{Z}_u^* = (P^T\tilde{\Sigma}^2P)^{-1}P^T\tilde{\Sigma}^2\tilde{\Gamma}$.

A.4 Network Structure Details

In this part, we introduce the detailed structure of our network. In general we set the kernel size of convolutional layers to be 3 unless otherwise stated.

(a) Encoder. We adopt the Swin-Large (Liu et al., 2021b) as our backbone. The network first divides the image into patches each of size 4×4, and embeds each patch into a 96-dimensional vector. The above procedure is implemented by a convolutional layer with kernel size 4 and stride 4. Then there are 4 transformation stages to be applied to the embedded vector. The first, second, third and forth stages include $2, 2, 18, 2$ blocks, respectively. More specifically, each block will divide the feature map into non-overlapped windows of size 12×12 , and compute new features within each window following the transformer (Vaswani et al., 2017). The feature channels in the 4 stages are 192, 384, 768 and 1536, respectively, and the number of heads are 6, 12, 24, and 48, respectively. In the end of each stage, there will be a downsampling operation to reduce the resolution of the feature map by 2. We collect the feature map before the downsampling operation as the output of the stage. In the end, the strides of output feature maps are 4, 8, 16, and 32 respectively. And the channels are 192, 384, 768, and 1536, respectively.

(b) Upsampling 32->16. Given the feature maps of strides 32 and 16 from **(a)**, we first upsample the feature map of stride 32 to stride 16 via bi-linear interpolation. Then, we concatenate the feature maps and obtain a new feature map of stride 16 and channels $1536 + 768 = 2304$. We apply a convolutional layer that has 2304 input channels, 2304 output channels, and 4 groups, to fuse the information. We also append an instance normalization layer (Ulyanov et al., 2016) and a LeakyReLU activation function. Next, we apply another convolutional layer with 2304 input channels, 512 output channels to compress the feature channels. Again we append an instance normalization layer and the LeakyReLU activation function. In the end, we add a skip connection between the result feature map and the previous concatenated feature map by addition operation. The concatenated feature map will be transformed to consistent number of channels in advance by a convolutional layer with 2304 input channels and 512 output channels. The final feature map has stride 16 and 512 channels.

(c) V-Layer. The V-layer takes the output feature map from **(b)** as input. We first utilize a convolutional layer with 512 input channels and 512 output channels to transform the feature map into a more appropriate hidden space. The feature is transformed by the LeakyReLU activation function. Then we utilize another convolutional layer with 512 input channels and $2 \times 16 = 32$ output channels to predict the gradients along the horizontal and vertical axis, respectively. The number 16 represents that we predict 16 channels of horizontal gradients and 16 channels of vertical gradients respectively, where each channel is expected to capture different information in scenes. Similarly, we also use another convolutional layer with 512 input channels, $2 \times 16 = 32$ output channels to predict the corresponding confidence weight maps. The confidence weight will be transformed by the Sigmoid function. Then we reshape the predictions and compute the unscaled depth map for

each pair of gradient and confidence weight following Eq.(5). The unscaled depth maps computed from all the pairs will be concatenated along the channel. Thereby we obtain a depth map with 16 channels and stride 16. We apply a group normalization on the depth map, where the 16 channels are viewed as a single group. In the end, we expand the channels of the depth map into 128 by a convolutional layer. Thereby the output of the V-layer is a depth map with 128 channels and stride 16.

(d) Refine 16. We refine the feature map from **(b)** and the depth map from **(c)**. Specifically, we first concatenate the feature map with depth map, and obtain a new feature map with $512 + 128 = 640$ channels. Then we employ a convolutional layer with 640 input channels and 640 output channels to fuse the information. The result feature map will be further transformed by the LeakyReLU activation function. Next a convolutional layer with 640 input channels and 128 output channels is applied to predict the refined depth map. Similarly, we also predict the refined feature map by a convolutional layer with 640 input channels and 512 output channels.

(e) Upsampling 16->8. Here, we upsample the feature map from **(d)** to stride 8 via bi-linear interpolation. To recover the information of scenes, we concatenate with the feature map from the encoder that has the same stride. In such a way, we obtain a new feature map with $384 + 512 = 896$ channels and stride 8. Similar to **(b)**, we apply a convolutional layer with 896 input channels, 896 output channels, and 4 groups to fuse the information. Then the feature map is transformed by the instance normalization layer and the LeakyReLU activation function. Next, we apply another convolutional layer with 896 input channels and 256 output channels to compress feature channels. Again, we apply the instance normalization layer and LeakyReLU activation function. Same as **(b)**, we add a skip connection between the result feature map and the previous concatenated feature map by addition operation. The concatenated feature map will be transformed to the consistent number of channels by a convolutional layer with 896 input channels and 256 output channels. Thereby the final feature map has stride 8 and 256 channels.

(f) Refine 8. We refine the depth map from **(d)** and the feature map from **(e)**. The procedure is the same as **(d)**, except for the number of channels in convolutional layers are adapted accordingly. Thereby we introduce the pipeline briefly. We first upsample the depth map from **(d)** into stride 8 to concatenate with the feature map. Thereby we obtain a new feature map with $256 + 128 = 384$ channels. Then, we apply a convolutional layer with 384 input channels and 384 output channels to fuse the information. The feature map is then transformed by LeakyReLU activation function. Next, we utilize a convolutional layer with 384 input channels and 128 output channels to predict the refined depth map. Similarly, another convolutional layer with 384 input channels and 256 output channels is applied to predict the refined feature map.

(g) Upsampling 8->4. We upsample the feature map from **(f)** to stride 4. The procedure is the same as **(e)** except for the number of channels. More specifically, we first upsample the feature map and concatenate with the feature map from the encoder with consistent stride, obtaining a feature map with $256 + 192 = 448$ channels and stride 4. Then a convolutional layer with 448 input channels, 448 output channels, and 4 groups is applied to fuse the information. Then the result feature map is transformed by the instance normalization and LeakyReLU activation function. Next, we apply another convolutional layer with 448 input channels and 64 output channels to compress the feature channels. Again, the instance normalization layer and LeakyReLU function is applied. In the end, we add a skip connection between the final feature map and the previous concatenated feature map.

(h) Refine 4. We refine the depth map from **(f)** and the feature map from **(g)** following the same pipeline as **(d)**. We first upsample the depth map to stride 4, and concatenate with the feature map, obtaining a new feature map with $64 + 128 = 192$ channels and stride 4. Next, we apply a convolutional layer with 192 input channels and 192 output channels to fuse the information, and a LeakyReLU function to transform the feature map. In the end, we utilize another convolutional layer with 192 input channels and 128 output channels to predict the new depth map. The output is a depth map with 128 channels and stride 4.

(i) Metric Layer. We take the feature map with stride 32 from the encoder as input. We first apply global max pooling to compress the feature map into a vector with 1536 channels. Then we apply a fully-connected layer with 1536 input units and 384 output units to compress the channels. Next we apply a LeakyReLU function. In the end, we utilize another fully-connected layer with 384 input units and 2 output units to regress the scale and shift.

Table 9: Comparison with Ramamonjisoa et al. (2020), Cheng et al. (2018) and Li et al. (2017) on NYU Depth V2 test set (Silberman et al., 2012).

Method	SILog ↓	Abs Rel ↓	RMS↓	RMS log↓	δ_1 ↑	δ_2 ↑
Ramamonjisoa et al. (2020)	8.655	0.088	0.320	0.113	0.929	0.991
Cheng et al. (2018)	8.640	0.089	0.317	0.112	0.930	0.991
Li et al. (2017) (end-to-end)	8.557	0.088	0.315	0.112	0.931	0.991
Li et al. (2017) (optimization)	8.574	0.089	0.316	0.112	0.930	0.991
Ours	**8.198**	**0.086**	**0.304**	**0.108**	**0.937**	**0.992**

Table 10: **Impact of resolution**. We evaluate the performance of V-layer when operating on feature maps of stride 16 and 8, respectively.

Stride	FPS↑	SILog ↓	Abs Rel ↓	RMS↓	RMS log↓	δ_1 ↑	δ_2 ↑
16	**7.032**	8.198	**0.086**	**0.304**	**0.108**	**0.937**	**0.992**
8	2.597	**8.149**	**0.086**	0.306	**0.108**	0.936	**0.992**

(j) Final Prediction. We take the output from **(d)**,**(f)**, **(h)** and **(i)** as input. We upsample all the depth maps to stride 1 via bi-linear interpolation, and fuse the depth maps into a single depth map by the addition operation and a convolutional layer with 128 input channels and 1 output channel. In the end, we add the depth map with the shift and multiply with the scale from **(i)**, respectively.

A.5 Statistical Evaluation With Other Methods

In this section, we compare with Ramamonjisoa et al. (2020), Cheng et al. (2018), and Li et al. (2017) on NYU Depth V2 (Silberman et al., 2012). More specifically, we apply their methods to refine the final predicted depth map. The displacement field, the affinity matrix, and the depth gradient are predicted from the refined feature map, which is the output of the last refinement module. For Cheng et al. (2018) we adopt their default hyper-parameters. The kernel size is 3, and the number of iterations is 24. Li et al. (2017) proposes the end-to-end fusion strategy and the optimization-based fusion strategy. For the end-to-end fusion strategy, we employ three convolutional layers with kernel size 5, and 16 channels. For the optimization-based fusion strategy, we use Adam optimizer. The learning rate is 0.01 and the number of iterations is 100. The results are shown in Tab. (9). Our method achieves better performance.

A.6 Ablation on Resolution

In this part, we evaluate the performance of the V-layer when applying on the feature map with stride 8. We achieve this by dividing the feature map into 4 rectangle sub-regions with equal area (top left, top right, bottom left and bottom right). We apply a V-layer on each sub-region. The predicted depth maps from the sub-regions will be stacked to recover the original resolution. The results are shown in Tab.(10). From stride 16 to 8, the improvement of accuracy is marginal. However, the inference speed (FPS) is significantly slow down.

A.7 Ablation on KITTI and SUN RGB-D

To further demonstrate the benefits of our V-layer on KITTI Eigen split (Geiger et al., 2012; Eigen et al., 2014) and SUN RGB-D test set (Song et al., 2015), we present the accuracy of the predicted depth map when replacing the V-layer with a single convolutional layer. As shown in Tab.(11), our V-layer can improve the depth map accuracy on both KITTI and SUN RGB-D.

Table 11: **Benefit of V-layer.** We replace the proposed V-layer with a single convolutional layer, and evaluate the predicted depth map accuracy.

Dataset	Layer	SILog ↓	Abs Rel ↓	RMS↓	RMS log↓	δ_1 ↑	δ_2 ↑
KITTI	Convolution	6.996	0.052	0.217	0.079	0.975	**0.997**
	V-Layer	**6.817**	**0.050**	**0.209**	**0.076**	**0.977**	**0.997**
SUN	Convolution	13.172	0.098	0.309	0.132	0.924	0.981
	V-Layer	**12.596**	**0.094**	**0.299**	**0.127**	**0.929**	**0.983**

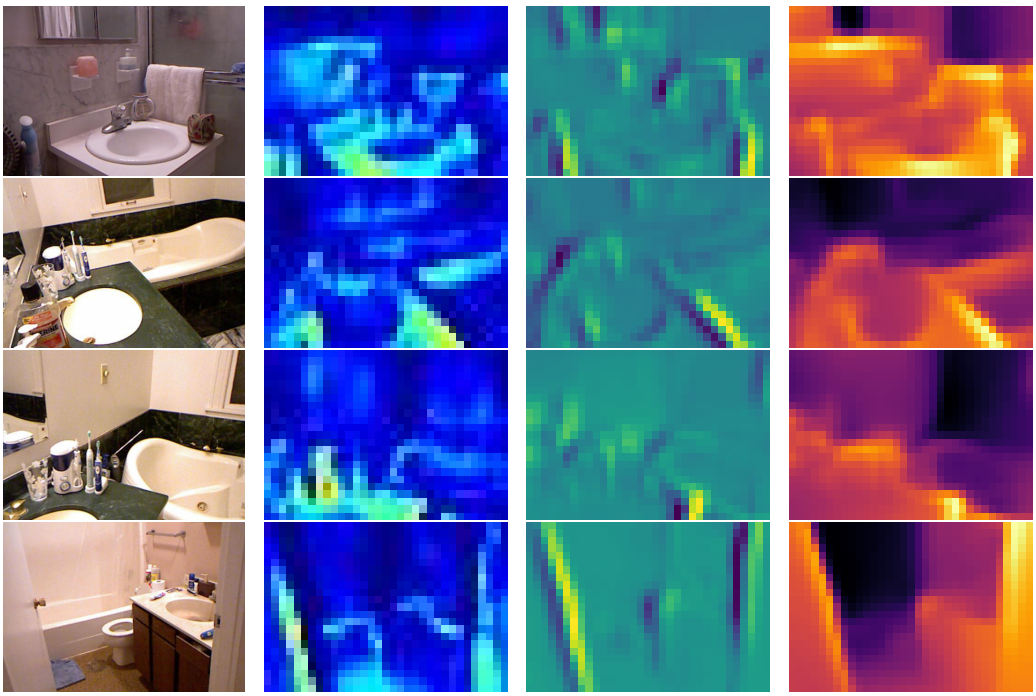

(a) Image (b) Confidence Weight (c) Difference Map (d) Depth Map

Figure 5: **Visualization of V-layer Prediction.** We visualize the confidence weight Σ_x, the difference map Γ_x and the depth map Z_u from the V-layer when predicting on NYU Depth V2 test set.

Table 12: Comparison with AdaBins and NeWCRFs on NYU test set. All methods are trained on KITTI Eigen train set without fine-tuning on NYU.

Method	Backbone	SILog ↓	Abs Rel ↓	RMS↓	RMS log↓	δ_1 ↑	δ_2 ↑
AdaBins(Bhat et al., 2021)	EffNet-B5+ViT-mini	28.147	0.251	0.753	0.286	0.614	0.867
NeWCRFs (Yuan et al., 2022)	Swin-L	21.138	0.173	0.551	0.213	0.755	0.934
Ours	Swin-L	**18.090**	**0.148**	**0.474**	**0.182**	**0.804**	**0.955**

A.8 More Generalization Experiments

We further evaluated the generalization performance when training on KITTI and test on NYU, or training on NYU and test on KITTI. The results are shown in Tab.(12) and Tab.(13). Our method achieves better generalization performance in both settings.

Table 13: Comparison with AdaBins and NeWCRFs on KITTI Eigen test set. All methods are trained on NYU Depth V2 train set without fine-tuning on KITTI Eigen.

Method	Backbone	SILog ↓	Abs Rel ↓	RMS↓	RMS log↓	δ_1 ↑	δ_2 ↑
AdaBins(Bhat et al., 2021)	EffNet-B5+ViT-mini	56.871	0.350	7.221	0.579	0.434	0.744
NeWCRFs (Yuan et al., 2022)	Swin-L	54.460	0.268	6.246	0.550	0.512	0.833
Ours	Swin-L	**42.105**	**0.221**	**5.360**	**0.426**	**0.598**	**0.888**

A.9 Sparse Ground-Truth Depth Map

KITTI provides sparse LiDAR measurements as the ground truth (official ground truth has been inpainted to an extent). Yet, our method could work well in such cases where sparse LiDAR measurements are known. Our algorithm computes the depth map from the gradient predicted by the network in a differentiable way. Thereby, for such a case, when we apply sparse supervision on the computed depth map (note that the loss function is used for valid measurements only), the error signal from the loss function will be back-propagated to the predicted gradient to supervise the network

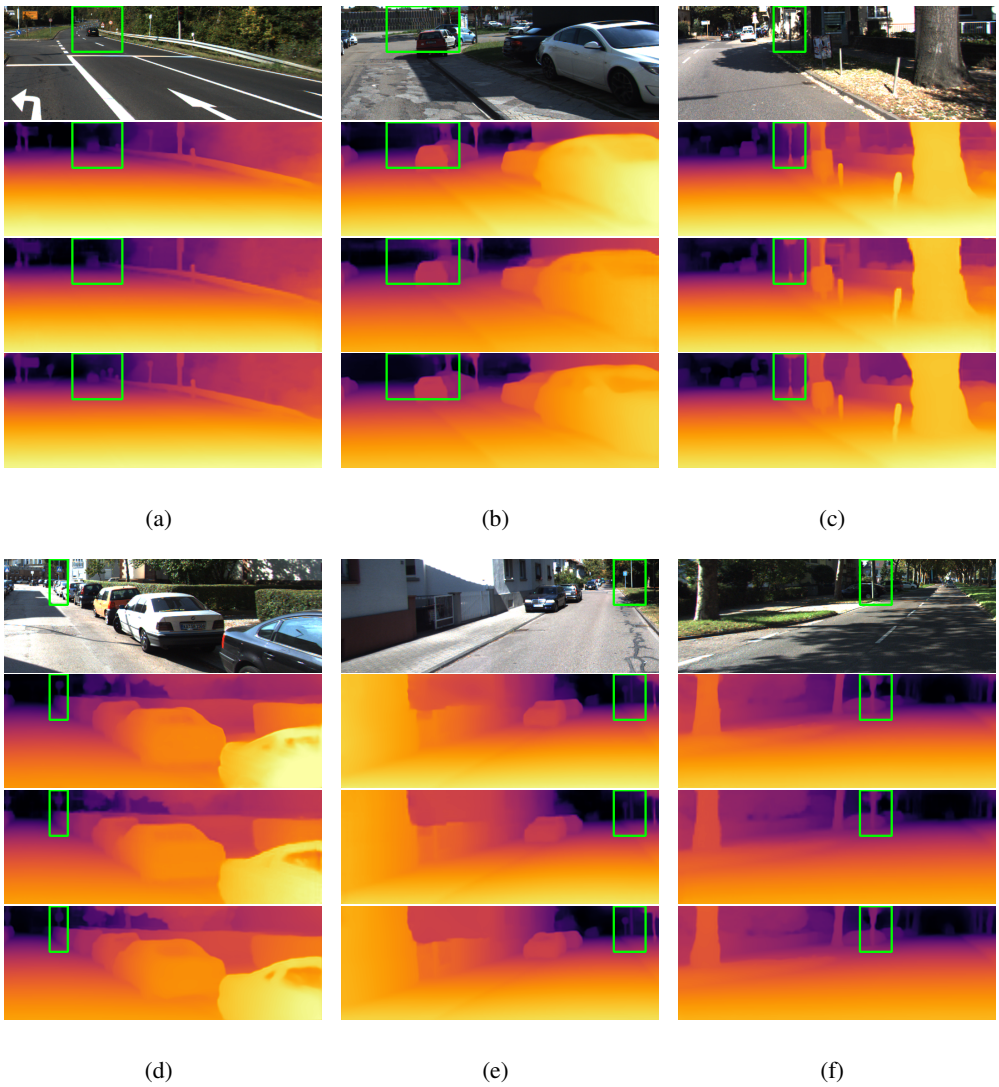

Figure 6: Qualitative comparison on KITTI Eigen split (Eigen et al., 2014). For each column, from top to bottom we present the input image, the prediction from AdaBins (Bhat et al., 2021), NeWCRFs (Yuan et al., 2022), and our framework respectively.

to learn gradient clues. We demonstrated the effectiveness of our algorithm in Tab.(2) and Tab.(3) for such cases.

A.10 More Visualization

We visualize the confidence weight map Σ_x, the difference map Γ_x, and the depth map Z_u from the V-layer in Fig.5. We observe that the depth value of a pixel shows correlation with respect to the image coordinates of the pixel. For example, in the last example in Fig.5, for different pixels at the door, the depth values are usually different but the first order difference are approximately the same. This observation shows that the difference map might be easier to predict than the depth map.

A.11 Qualitative Results

We provide more qualitative results on KITTI Eigen split (Eigen et al., 2014), SUN RGB-D (Song et al., 2015), and NYU Depth V2 (Silberman et al., 2012) in Fig.6, Fig.7 and Fig.8, respectively. Our framework predicts more accurate shapes and preserves the high-frequency scene information.

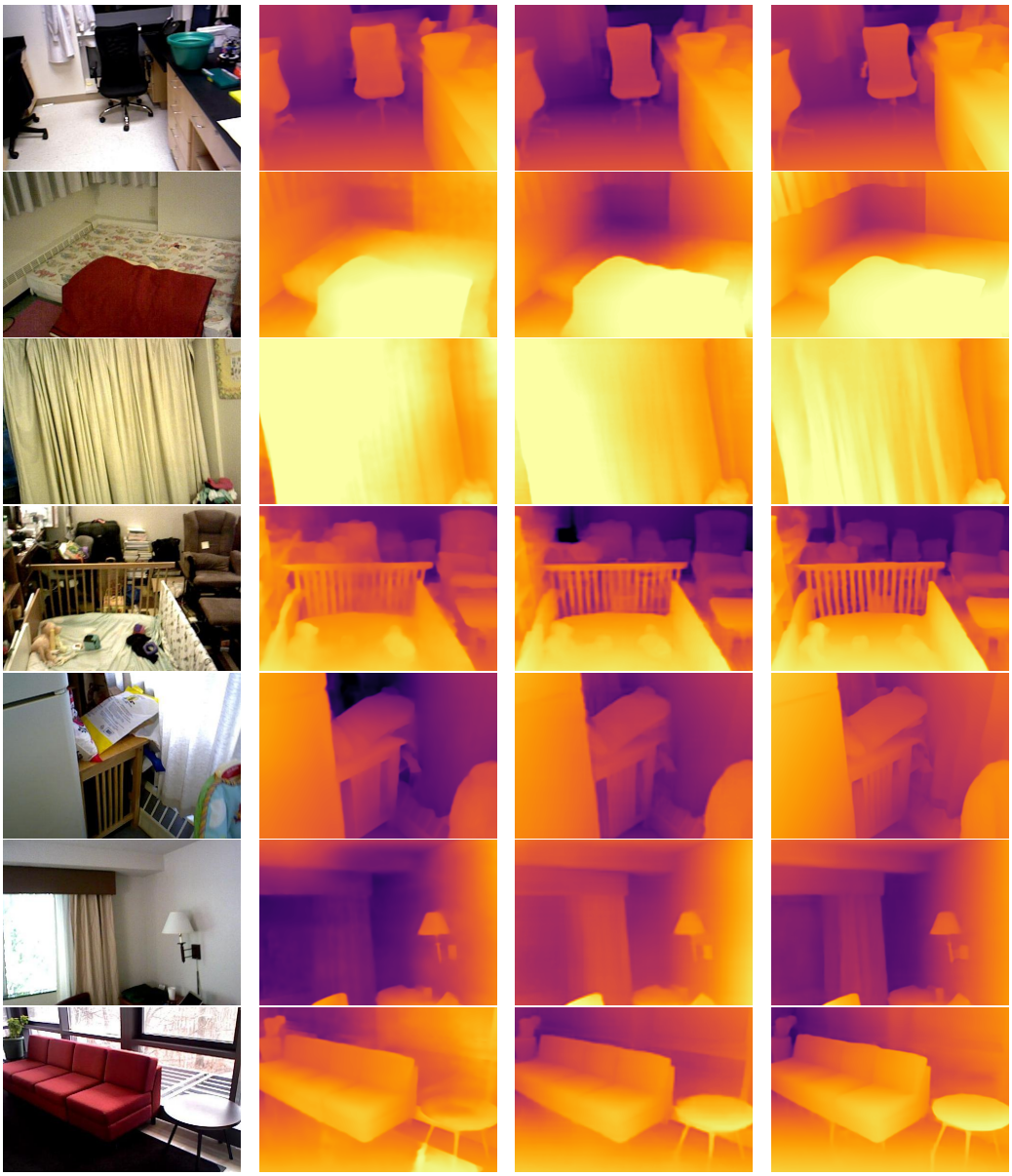

(a) Image (b) AdaBins (c) NeWCRFs (d) Ours

Figure 7: Qualitative comparison with AdaBins (Bhat et al., 2021), NeWCRFs (Yuan et al., 2022) on SUN RGB-D test set (Song et al., 2015). All the models are pre-trained on NYU Depth V2 (Silberman et al., 2012) training set.

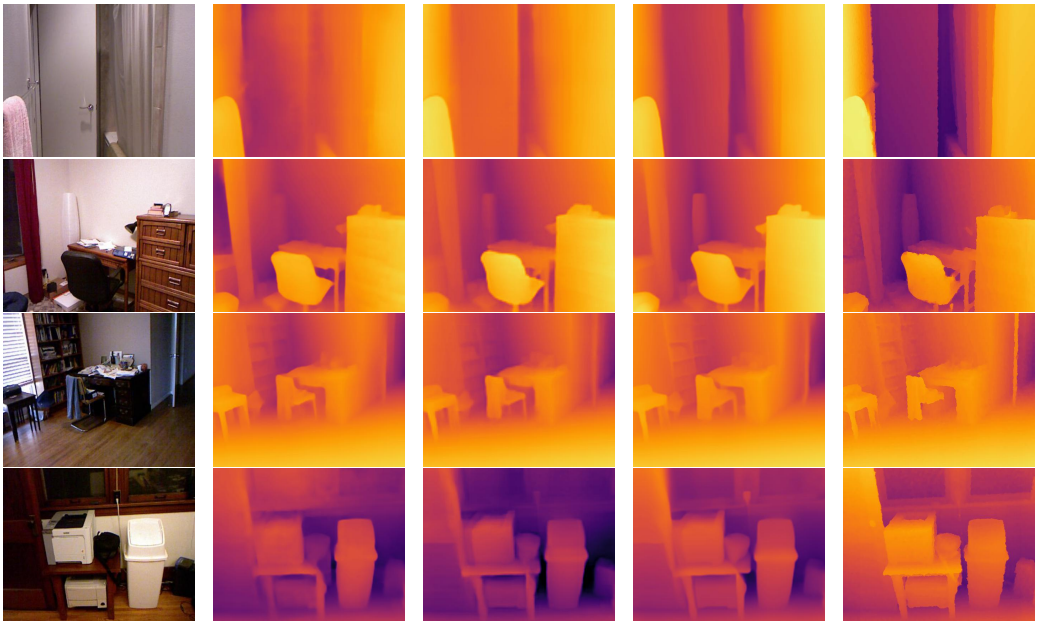

(a) Image (b) AdaBins (c) NeWCRFs (d) Ours (e) Ground Truth

Figure 8: Qualitative comparison with AdaBins (Bhat et al., 2021), NeWCRFs (Yuan et al., 2022) on NYU Depth V2 test set (Silberman et al., 2012). The ground-truth depth map are in-painted for visualization.